



Cite this: *Phys. Chem. Chem. Phys.*, 2026, **28**, 6963

Solvent-accelerated photoreduction of Hg(II) dihalides: uncovering solvent-governed and light-triggered mercury chemistry

Donghwan Im, ^{†ab} Alekos Segalina ^{†ab} and Hyotcherl Ihee ^{*ab}

Mercury dihalides (HgX₂, X = Cl, Br, I) undergo photoreduction much more rapidly in aqueous environments than in the gas phase. Using *ab initio* molecular dynamics simulations and high-level electronic structure calculations, we investigate how solvation shapes the molecular structure, electronic distribution, and excited-state character of HgX₂ complexes. We find that strong Hg–solvent interactions induce pronounced deviations from linear geometries and lead to partial negative charge accumulation on HgX₂ in polar solution. Moreover, we identify that the second absorption band in the deep-UV region exhibits a strong solvent-to-solute charge-transfer (CT) character. Combining the accumulation of partial negative charge in the ground state with the enhanced solvent-to-solute CT character promotes efficient electron localization on the Hg center after photoexcitation, thereby accelerating photoreduction in solution. By providing atomistic insight into solvation-driven excited-state reactivity, this work establishes the molecular basis for the accelerated photochemistry of HgX₂ in aqueous media and underscores the essential role of explicit solvation in modeling the solution-phase photochemistry of mercury species relevant to the global mercury cycle.

Received 5th December 2025,
 Accepted 23rd February 2026

DOI: 10.1039/d5cp04729c

rsc.li/pccp

Introduction

Mercury (Hg) is a globally pervasive toxic pollutant, exerting profound impacts on both human and ecological health. Atmospheric mercury primarily exists as elemental mercury vapor (Hg(0)) and particulate-bound or dissolved divalent mercury (Hg(II)). While Hg(0) accounts for over 95% of total atmospheric mercury due to its long atmospheric lifetime and global mobility, Hg(II) is far more reactive and water-soluble, making it the primary species deposited to aerosols, snowpacks, and oceans.^{1,2} The global atmospheric mercury burden derives from both natural and anthropogenic origins. Natural processes such as volcanic activity and the re-emission of previously deposited mercury from soils and oceans account for roughly two-thirds of the total while the remaining one-third stems from primary anthropogenic emissions, mainly from coal combustion, metal smelting, and other industrial activities.^{3–6}

The interconversion between Hg(0) and Hg(II) through redox reactions governs mercury's atmospheric lifetime, long-range transport, and eventual deposition, thereby playing a central

role in the global mercury cycle.⁷ During polar springtime, photochemical activation of sea salt aerosols produces reactive halogens, initiating Atmospheric Mercury Depletion Events (AMDEs), in which Hg(0) is rapidly converted into oxidized mercury species such as HgBr₂. Halogen-mediated oxidation and reduction of Hg, particularly involving bromine radicals, has emerged as the dominant pathway in the polar and marine boundary layers.^{8,9} While bromine has been the primary focus of the halogen-mediated oxidation pathway, recent observations highlight the growing importance of chlorine and iodine in the redox cycle of Hg, particularly in Arctic environments.^{10–12} Elevated tropospheric iodine levels have been detected over continental and polar regions, and halogen-containing mercury species such as HgCl₂ and HgI₂ are increasingly implicated in the oxidative transformation and deposition of atmospheric Hg(0).¹³ Quantum chemical studies further indicate that iodine-based oxidation pathways are thermodynamically viable and may even outcompete bromine under certain conditions.¹⁴ Collectively, these findings point to halogens as key agents in atmospheric mercury redox cycling, leading to the formation of HgX₂ species (X = Cl, Br, I) whose persistence and reactivity hinge on downstream photochemical processes.

Once formed, HgX₂ compounds can undergo photoreduction upon exposure to sunlight, releasing Hg(0) back into the atmosphere. Here, photoreduction denotes a direct, catalyst-free, light-driven process in which photoexcitation of HgX₂

^a Department of Chemistry, Korea Advanced Institute of Science and Technology (KAIST), Daejeon 34141, Republic of Korea. E-mail: hyotcherl.ihee@kaist.ac.kr

^b Center for Advanced Reaction Dynamics (CARD), Institute for Basic Science (IBS), Daejeon 34141, Republic of Korea

[†] Both authors contributed equally to this work.



weakens the Hg–X bonds, promotes Hg–X bond cleavage to form HgX[•] radicals, and ultimately results in the net conversion of Hg(II) to Hg(0) through both thermal and photochemical pathways. Recently, many studies have shown that photoreduction of HgBr₂ occurs much more rapidly in aqueous environments, including quasi-liquid layers (QLLs), stratospheric aerosols, and seawater, than in the gas phase.^{15,16} Notably, through high-level multiconfigurational calculations, recent a theoretical study reveals that the solvent environment can significantly enhance the intensity of absorption spectra and accelerate the photoreduction of HgX₂.¹⁷ However, key questions remain regarding the extent to which coordination of different solvent molecules to the Hg center alters the charge distribution of HgX₂, as well as how the surrounding solvent environment influences the local-excitation (LE) and charge-transfer (CT) character of electronic transitions in the UV–Vis region.

Beyond their environmental significance, HgX₂ molecules have attracted interest in ultrafast spectroscopy as prototypical systems for studying photodissociation dynamics.¹⁸ Femtosecond transient absorption (fs-TA) spectroscopy has shown that photoexcitation of HgX₂ in solution triggers homolytic bond cleavage into HgX[•] and X[•], with solvent-dependent vibrational coherences pointing to a key role of solute–solvent interactions in shaping the photochemical response.^{19–21} Also, time-resolved X-ray liquidography (TRXL),^{22–28} a structure-sensitive technique complementary to TA spectroscopy, has elucidated the structural dynamics associated with the photodissociation and recombination dynamics of HgX₂ in solution, revealing both two-body and three-body dissociation channels and the subsequent formation of Hg(0) and X₂.^{29–31}

From a theoretical chemistry perspective, an accurate description of solute–solvent interactions require moving beyond implicit solvent models to full quantum mechanical treatments. Yet, because of the considerable computational cost associated with explicit solvent treatments, solvent effects are most often captured using simplified implicit models. Still, explicit treatment of solvent molecules is crucial for deciphering how local solvation governs photochemical behavior, including electronic structure mixing between HgX₂ and surrounding solvent molecules, as well as the resulting reactivity of Hg species in solution. These factors, in turn, critically influence their environmental transformation pathways, long-range transport potential, and ultimate fate within diverse natural water bodies.

In this work, we integrate *ab initio* molecular dynamics (AIMD) simulations with excited-state electronic structure calculations to investigate the photophysical properties of HgX₂ in solution. By computing absorption spectra using a fully quantum-mechanical treatment of surrounding solvent molecules and analyzing their structural origins across multiple solvents, we provide atomistic insight into how strong solute–solvent interactions induce partial negative charge accumulation in the ground state and promote solvent-to-solute CT character in the UV-vis spectra of HgX₂. These effects collectively shape the excited-state landscape of HgX₂ complexes in

solution, thereby bridging the gap between gas-phase and solution-phase dynamics relevant to atmospheric and cryospheric mercury cycling.

Computational details

Molecular dynamics simulations

To investigate solute–solvent interactions of HgX₂ molecules under polar conditions, AIMD simulations were performed. Each system was prepared in a cubic box of 20 Å per side with periodic boundary conditions, using the experimental bulk densities of the four solvents: water (0.997 g cm⁻³), methanol (MeOH, 0.793 g cm⁻³), pyridine (0.982 g cm⁻³), and dimethyl sulfoxide (DMSO, 1.100 g cm⁻³). Solvent molecules were first packed into the box using the Packmol software,³² and one solvent molecule was then replaced with an HgX₂ molecule. From those boxes, initial geometry optimization was carried out for 25 steps to remove unfavorable contacts. For the subsequent step, equilibration was carried out in two stages under the NVT ensemble using the Nosé–Hoover thermostat:^{33,34} the first for 2 ps with a thermostat time constant of 50 fs, followed by a second 5 ps run with a 200 fs thermostat time constant, both at 300 K. The convergences of temperature throughout the AIMD simulations for all systems are shown in Fig. S1–S3. Final production runs were performed for 5 ps. To ensure statistical robustness, three independent AIMD simulations were conducted for each system, yielding a total of 15 ps of production data per solvent. Fig. S4 shows the evolution of the time-averaged X–Hg–X bond angles as a function of the cumulative length of the sampled trajectories, demonstrating the convergence of the corresponding structural parameters.

All AIMD simulations were performed using the PBE exchange–correlation functional, with D3 dispersion corrections applied within a 9 Å cutoff.^{35,36} The TZV2P-MOLOPT basis set was employed in combination with the GTH-PBE-q12 pseudopotential for the description of the Hg atom, and similarly, the TZV2P-MOLOPT basis set and the GTH-PBE-q7 pseudopotential were used for halogens.³⁷ The solvent molecules were described using the DZVP-GTH basis set along with the corresponding GTH pseudopotentials. A plane-wave cutoff of 600 Ry and a relative cutoff (REL_CUTOFF) of 60 Ry were used for the auxiliary plane-wave basis. Additionally, scalar relativistic effects were included *via* the zeroth-order regular approximation (ZORA) Hamiltonian, scaled with an atomic model potential. All AIMD simulations were performed using the CP2K 8.2 package.³⁸ From the trajectories, we calculate the coordination number of the Hg–solvent pair, defined as

$$\text{Coordination number} = 4\pi\rho\int r^2g(r)dr, \quad (1)$$

where ρ is the number density of the Hg–O (or Hg–N) pair in the solvent, and $g(r)$ is the radial distribution function (RDF) of that pair.



Geometry classification from trajectory analysis

To assess the coordination environment of HgX_2 molecules in the solution phase, we analyzed structural features extracted from the AIMD trajectories. For each sampled trajectory frame, we identified the Hg atom, its two halogen ligands, and the two closest donor atoms, and computed six unique L–Hg–L angles ($L = X$ or O/N). Geometric deviations were quantified using an angle deviation metric (ADM), defined as (2), which indicates absolute deviation from ideal angles associated with tetrahedral (109.5°), square planar (180° , 90°), and T-shaped (180° , 90°) geometries.

$$\text{ADM} = \frac{1}{N} \sum_{i=1}^N |\theta_i - \theta_i^{\text{ref}}| \quad (2)$$

here, θ_i is the i th measured L–Hg–L angle, and θ_i^{ref} is the corresponding ideal angle for the reference geometry.

Calculation of the excited state properties and absorption spectra

For detailed assignment of the absorption spectra and comparison with time-dependent density functional theory (TD-DFT) calculations, we performed extended multi-state complete active space second-order perturbation theory (XMS-CASPT2) calculations based on state-averaged complete active space self-consistent field (SA-CASSCF) wavefunctions with an active space of CAS(12e, 10o), incorporating 12 singlet and 12 triplet states for the state-averaging process (see Fig. S5 for active space orbitals). The ANO-RCC-VTZP basis set was used throughout.³⁹ To address the intruder state problem, which is commonly encountered in multi-state CASPT2 calculations, an imaginary level shift of 0.25 au was applied.⁴⁰ Relativistic effects were considered employing the second-order Douglas–Kroll–Hess (DKH2) Hamiltonian combined with the atomic mean-field integral (AMFI) approach.^{41,42} To accelerate the speed of simulations, the resolution-of-the-identity Cholesky decomposition (RICD) technique was employed.⁴³ We note that all multiconfigurational calculations were performed without consideration of any solvent effects. Excitation energies, oscillator strengths, and the composition of spin–orbit free (SF) states in spin–orbit coupled (SO) states were obtained using the RASSI module, as implemented in the OpenMolcas v25.02 package.⁴⁴

TD-DFT calculations were performed using the CAM-B3LYP functional with D3 dispersion corrections.⁴⁵ The relativistic effects were treated with the exact two-component (X2C) Hamiltonian, employing the X2C-TZVPall basis set and the corresponding X2C/J auxiliary basis set.⁴⁶ We note that the excitation energies and the nature of the electronic transitions obtained from XMS-CASPT2 and TD-DFT calculations are in good agreement. Specifically, as shown in Fig. S6, the vertical excitation energies calculated at the XMS-CASPT2 and CAM-B3LYP levels differ by no more than ~ 0.3 eV and exhibit identical electronic transition character for the low-lying valence excited states, in both linear and bent configurations.

To investigate the influence of solvent treatment on the spectral properties, representative snapshots of HgX_2 and surrounding solvent molecules were obtained from the AIMD simulation trajectories. In total, 300 snapshots, including 50 water or 30 MeOH molecules around HgX_2 , were stochastically extracted from the production runs, with 100 geometries sampled from each of the three independent 5 ps trajectories. Absorption spectra were then calculated from these snapshots using the nuclear ensemble approach (NEA) proposed by Barbatti *et al.*,⁴⁷ employing three different treatments: (i) without any solvent effects (Gas), (ii) with an implicit solvation model (Truhlar's SMD model⁴⁸), (iii) employing hybrid QM/MM approach and (iv) with explicit inclusion of nearby solvent molecules in the quantum mechanical (QM) region together with the implicit SMD model. In the QM/MM calculations, water molecules were described using the TIP3P model, while methanol parameters were taken directly from the OPLS-AA force-field database without further reparameterization. Additionally, to assess the effect of geometrical distortions on the absorption spectra, two sets of spectra were calculated using the NEA approach: one from geometries sampled *via* the Wigner distribution based on the linear gas-phase structures, and the other from geometries obtained through AIMD simulations. For all absorption spectra calculations, Lorentzian broadening with a full width at half maximum (FWHM) of 0.2 eV was applied.

Mulliken charges in the ground state were calculated with CAM-B3LYP-D3/X2C-TZVPall (X2C-SVPall for solvent)/SMD level of theory from the sampled geometries with AIMD simulations. In the case of DMSO and pyridine, 15 nearby solvent molecules were included in the QM region and explicitly incorporated for the calculation. ORCA 6.0 package was employed for DFT and TD-DFT calculations,⁴⁹ and one-electron transition density matrix (1-TDM) analysis were performed with Theodore package.⁵⁰

Results and discussion

Structural and dynamic properties

To elucidate how HgX_2 complexes interact with different polar environments, we performed AIMD simulations in water and MeOH, representing polar protic solvents, and in pyridine and DMSO, which are polar aprotic solvents. To probe the local solvent environment in different solvents, we computed cumulated number density functions (CDFs) for the Hg–O pairs (or Hg–N for pyridine), which quantify the coordination number between the Hg atom in HgX_2 and the surrounding solvent O/N atoms, as shown in Fig. 1. Regardless of halogen type or solvent environment, the calculated Hg–O/N coordination number remains close to 2 within 3.0 \AA , revealing the presence of a predominant two-coordinate solvation structure around HgX_2 . This Hg–O/N interaction is more pronounced in aprotic solvents than in protic ones, as evidenced by the higher Hg–O/N coordination numbers within a 2.5 \AA range. These results agree with experimental



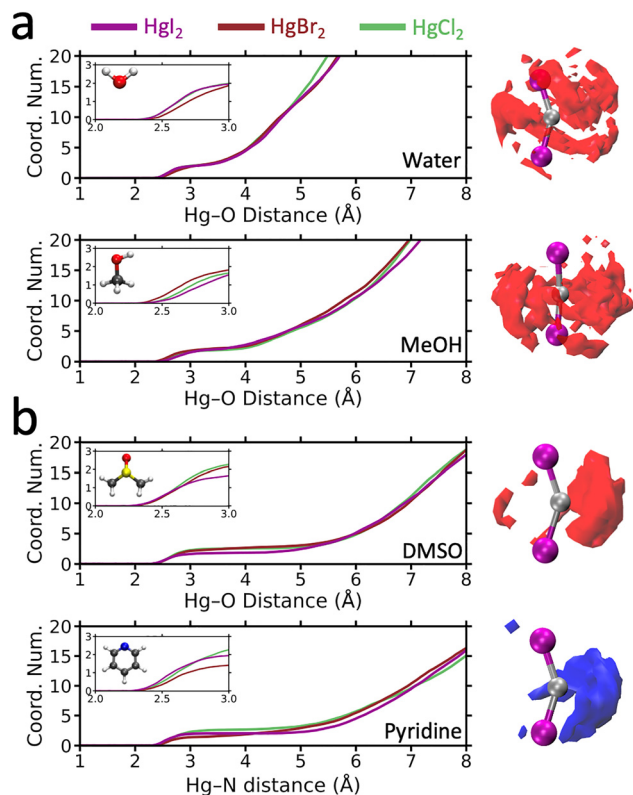


Fig. 1 Cumulative number density functions (CDFs) between Hg and oxygen (or nitrogen for pyridine) atoms, obtained from AIMD trajectories of HgX_2 molecules. The Hg–O/N coordination numbers were calculated in (a) protic solvents (water and MeOH), and (b) aprotic solvents (DMSO and pyridine). In each panel, the calculated Hg–O/N coordination numbers for HgCl_2 (green), HgBr_2 (brown), and HgI_2 (purple) are shown. Representative spatial distribution functions (SDFs) of O/N in each solvent are shown in the right panel. The insets show an enlarged view of the 2.0 to 3.0 Å region, highlighting the region of the first solvation shell. We note that the size of the second solvation shell is correlated with the size of the solvent molecule: smaller sizes of solvent tend to form the second shell at shorter distances and *vice versa*.

studies pointing to enhanced complexation of HgX_2 in aprotic solvents.^{51,52}

Although $\text{Hg}(\text{II})$ can coordinate with oxygen lone pairs, in protic solvents such as water and MeOH, extensive halogen bonding networks compete with direct Hg–O coordination, thereby reducing the stability and persistence of solute–solvent interactions. Therefore, beyond Hg–O/N interactions, we also examined the strength of halogen bonding with hydrogen-bond donors by computing CDFs for halogen–hydrogen pairs (Fig. S7). The CDFs reveal that halogen bonding contributes to HgX_2 solvation in both protic solvents, as evidenced by non-zero values within 3.0 Å for all halogens; however, its magnitude is much lower than that of Hg–O/N interactions, suggesting that halogen bonding plays only a minor role in modulating the structural properties of HgX_2 .

To assess the impact of Hg–O/N interactions on the geometry of HgX_2 , we analyzed the conformations of HgX_2 across different solvents. Table 1 summarizes the average Hg–X bond lengths and X–Hg–X angles for all halogen species and solvent

environments, together with available experimental and theoretical data. Across all cases, a slight elongation of the Hg–X bond is observed in solution compared to the gas phase, reflecting the influence of Hg–O/N interactions on the coordination geometry. Compared to the optimized linear structure of HgX_2 in the gas phase, the solvated HgX_2 complexes exhibit Hg–X bond lengths elongated by 0.06–0.14 Å, depending on the halogen and the solvent (see Table 1 and Fig. S8–S10). This bond elongation is more pronounced in aprotic solvents than in protic ones. This trend can be attributed to solvent-induced changes in the local coordination environment of Hg, particularly interactions with electronegative O or N atoms. Such interactions can alter the electron density around the Hg atom and reduce the covalent character of the Hg–X bond, leading to its elongation. This interpretation aligns with previous experimental and theoretical studies that have reported similar solvent-induced elongation of Hg–Br and Hg–Cl bonds in solution.^{53–56}

Importantly, population analysis shows that, HgX_2 acquires a partial negative charge upon solvation (see Table S1), evidencing significant electronic perturbation of HgX_2 occurs due to the significant Hg–O/N interaction. Although our simulations do not explicitly include anionic complexes, the elongation of Hg–X bonds observed for HgX_2 in polar solvents can be rationalized based on the behavior of HgX_2^- . The optimized geometry of HgX_2^- (see Table S2) and the calculated potential energy curves (PECs) for neutral HgI_2 and HgI_2^- (see Fig. S11) indicate that the additional negative charge weakens the Hg–X interactions, leading to bond elongation. This suggests that strong Hg–O/N interactions may shift the system toward a more anion-like bonding regime, thereby promoting structural destabilization relative to the neutral gas-phase counterpart. Nevertheless, the Hg–X bond lengths calculated from the AIMD simulations are slightly elongated relative to the values from experiment and high-level theoretical calculations, likely reflecting the limitations of the PBE functional, which lacks Hartree–Fock exchange. Employing hybrid functionals such as PBE0 within AIMD simulations could, in principle, improve the quantitative accuracy, albeit at a substantially higher computational cost.

In addition to bond elongation, our AIMD simulations also indicate that HgX_2 molecules in solution exhibit deviations from the linear structure, with some variations depending on the solvent. In protic solvents, the average X–Hg–X angle ranges from 155° to 165°, whereas in aprotic solvents, the structure exhibits a more pronounced bending with angles between 145° and 155°. This trend reflects the role of Hg–O/N interactions in modulating the structural flexibility of HgX_2 , with aprotic solvents, lacking a hydrogen-bonding network, and promoting stronger solute–solvent interactions and enhanced complexation, leading to greater bond elongation and angular deviations from linearity. These findings are consistent with previous X-ray diffraction and Raman studies on HgX_2 compounds in the solution phase, suggesting that HgX_2 can deviate from linearity due to Hg–O/N interaction, especially in O- and N-donor solvents such as DMSO and dimethylformamide (DMF).^{57–60}



Table 1 Comparison of calculated and experimental Hg–X bond distances and X–Hg–X angles of HgX₂ in the gas and solution phase

| Phase | HgI ₂ | | | HgBr ₂ | | | HgCl ₂ | | |
|----------|------------------|---|-----------------------------|---|-------------------------------|---|--------------------------------------|--|--|
| | | $r(\text{Hg-I})$ (Å) | $\angle(\text{I-Hg-I})$ (°) | $r(\text{Hg-Br})$ (Å) | $\angle(\text{Br-Hg-Br})$ (°) | $r(\text{Hg-Cl})$ (Å) | $\angle(\text{Cl-Hg-Cl})$ (°) | | |
| Gas | Calc. | 2.600 ^a , 2.527 ^b | 180.0 ^a | 2.414 ^a , 2.363 ^b | 180.0 ^a | 2.273 ^a , 2.230 ^b | 180.0 ^a | | |
| | Exp. | 2.568 ^c | 180 ^e | 2.384 ^c , 2.380 ^d , 2.41 ^e | 180 ^e | 2.252 ^c , 2.25 ^e | 180 ^e | | |
| Water | Calc. | 2.697 ± 0.048 ^a | 156.0 ± 5.4 ^a | 2.502 ± 0.052 ^a , 2.427 ^f | 159.8 ± 6.2 ^a | 2.373 ± 0.052 ^a , 2.333 ^f | 160.2 ± 6.8 ^a | | |
| | Exp. | — | — | 2.420 ^g | ~160 ^g | 2.29 ^g , 2.31 ^h | 174 ^e , ~160 ^g | | |
| MeOH | Calc. | 2.668 ± 0.046 ^a | 163.5 ± 4.7 ^a | 2.494 ± 0.046 ^a | 161.6 ± 5.6 ^a | 2.345 ± 0.041 ^a | 165.2 ± 5.2 ^a | | |
| | Exp. | — | — | — | — | 2.308 ^e , 2.30 ^h | 170 ^e | | |
| DMSO | Calc. | 2.705 ± 0.057 ^a | 148.6 ± 9.1 ^a | 2.522 ± 0.056 ^a | 158.0 ± 9.4 ^a | 2.401 ± 0.068 ^a | 157.6 ± 10.2 ^a | | |
| | Exp. | 2.625 ^e | 159 ^e | 2.455 ^e | 165 ^e | 2.32 ^e , 2.35 ^e | 165 ^e | | |
| Pyridine | Calc. | 2.716 ± 0.047 ^a | 145.2 ± 8.3 ^a | 2.508 ± 0.058 ^a | 158.1 ± 9.5 ^a | 2.410 ± 0.055 ^a | 155.5 ± 10.2 ^a | | |
| | Exp. | 2.665 ⁱ | 143 ⁱ | 2.497 ⁱ | 151 ⁱ | 2.375 ⁱ | 154 ^e | | |

^a This work. ^b Ref. 65. ^c Ref. 53. ^d Ref. 69. ^e Ref. 57. ^f Ref. 16. ^g Ref. 70. ^h Ref. 54. ⁱ Ref. 61.

To better characterize the solvent arrangement around each HgX₂ species, we computed the spatial density functions (SDFs) to visualize the preferred solvent positions (see the right side of Fig. 1). In aprotic solvents, the solvation shell appears more localized and asymmetric, with solvent molecules preferentially occupying specific regions around the complex, indicating the formation of directional, ligand-like interactions. In contrast, in protic solvents, HgX₂ shows smaller deviations from the 180° X–Hg–X angle and exhibits a more diffuse and isotropic distribution of surrounding molecules, with reduced directional preference and a more disordered solvation pattern. To quantify this directional solvation behavior, we assessed the degree to which the local solvent coordination around HgX₂ conforms to three idealized four-coordinate topologies: tetrahedral, T-shaped, and square planar. In Fig. 2, analysis *via* the ADM shows that, as the halogen size increases and in aprotic compared to protic solvents, the geometry of the HgX₂(solv)₂ complex progressively shifts from T-shaped toward a tetrahedral-like coordination. This reflects the enhanced directional Hg–O/N binding, a trend that was already qualitatively evident in the SDF analysis of Fig. 1. As the halogen size increases, the Hg–X bond weakens and the structure deviates

from linearity, suggesting a possible correlation between Hg–X bond strength and the resulting geometrical distortion and SDFs. In fact, the crystal structure of HgX₂(pyridine)₂ adopts a tetrahedral geometry with an X–Hg–X angle of approximately 110°.⁶¹ Based on these comparisons, HgX₂ complexes with lighter halogens in polar protic solvents tend to adopt geometries closer to linearity, whereas those with heavier halogens in aprotic solvents more closely resemble the crystalline tetrahedral form, albeit with weaker solvent coordination and minor structural distortion than in the crystal. Overall, our simulations demonstrate that in water and MeOH, HgX₂ molecules undergo more pronounced bending motions around the T-shaped structure, while in DMSO and pyridine they display stronger angular distortions of the X–Hg–X bond, approaching tetrahedral topology.

Nature of excited states and solvent effects on absorption spectra

To elucidate how the structural distortions induced by strong Hg–solvent interactions manifest under realistic conditions and modulate the photochemical properties of HgX₂, which readily undergoes photoreduction to form Hg(0), we characterized the nature of the excited states in the gas and solution phases. We analyzed the absorption spectra only in water and MeOH, as in DMSO and pyridine the strong solvent absorption and extensive electronic state mixing obscure the intrinsic spectral features of HgX₂ and require a level of excited-state sampling that cannot be adequately treated within the computational setup employed in this work. Also, in DMSO and pyridine, the deep-UV absorption is dominated by solvent-centered electronic transitions, which can lead to solvent photodissociation.

Fig. 3 presents the experimental absorption spectra of HgI₂ in the gas phase, water, and MeOH. Across all three environments, two main absorption bands are observed: a smaller peak at 4.5–5.0 eV and a larger peak at 5.5–6.0 eV. The key difference between gas-phase and solution spectra lies in the second band, which becomes markedly broadened and exhibits a pronounced blue-shift in both water and MeOH. To probe the origin of these spectral changes, particularly the link between peak broadening and solute–solvent interactions, we first

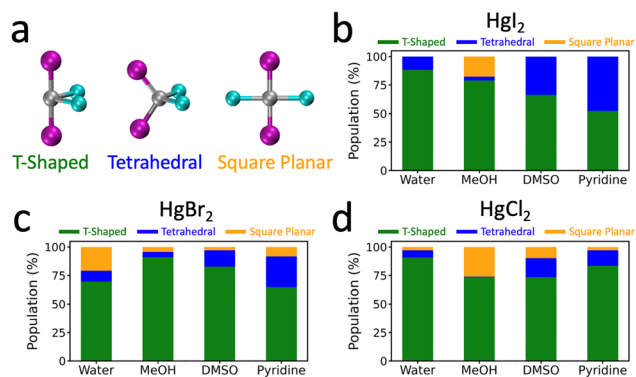


Fig. 2 (a) Three idealized coordination topologies of HgX₂(solv)₂ from AIMD simulations. (b–d) Portions of representative transient geometries from the AIMD simulations for (b) HgI₂, (c) HgBr₂, and (d) HgCl₂. Hg atoms are shown in silver, halogen atoms in purple, and coordinating solvent atoms in cyan. Structures in panel (a) serve as references for geometry classification.



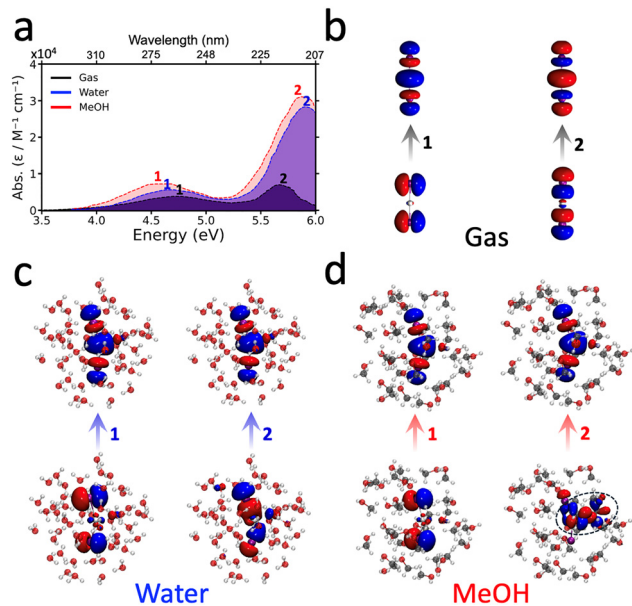


Fig. 3 Absorption spectra of HgI_2 measured in the gas phase,⁶⁶ in water⁶² and MeOH.⁶³ The normalized absorption spectra are provided in Fig. S17. Panels (b)–(d) display representative NTOs corresponding to the two main peaks observed in the experimental absorption spectra of HgI_2 in the gas phase, water and MeOH, respectively. In panel (d), the solvent orbital contributions to the transition underlying the second absorption peak are highlighted in a dashed circle.

analyzed the natural transition orbitals (NTOs) associated with the two principal absorption bands in the gas phase, water, and MeOH (Fig. 3b–d).

According to our calculations, the first absorption peak of gas-phase HgX_2 is predominantly characterized by an (n, σ^*) transition. The second band arises from a (σ, σ^*) excitation localized on the Hg–X bond, with additional halogen-to-metal charge transfer (XMCT) contributions from the halogen non-bonding p orbitals into the Hg 6p orbitals (see Tables S3–S11 for detailed characterizations). In solution, the first band retains its (n, σ^*) character; solvent effects here manifest primarily as a solvatochromic energy shift (*vide infra*), not a change in state character. By contrast, the second peak shows markedly different character, with solvent nonbonding orbitals contributing substantially to the excitation, particularly in MeOH. These contributions impart a pronounced solvent-to-solute CT character, thereby highlighting the decisive role of explicit solvation in modulating the electronic structure of the excited states of HgX_2 .

As a next step, to elucidate the role of the solvation in the absorption spectra of HgX_2 , we calculated absorption spectra from geometries extracted from the AIMD simulations, thereby incorporating structural disorder and finite-temperature effects. Briefly, absorption spectra were computed from AIMD snapshots of HgX_2 using three schemes designed to disentangle solute disorder from solvation effects: (i) gas-phase calculations of the isolated complex, (ii) inclusion of implicit solvation through Truhlar's SMD model,⁴⁸ (iii) QM/MM calculations in which solvent molecules are treated at the molecular mechanics level,

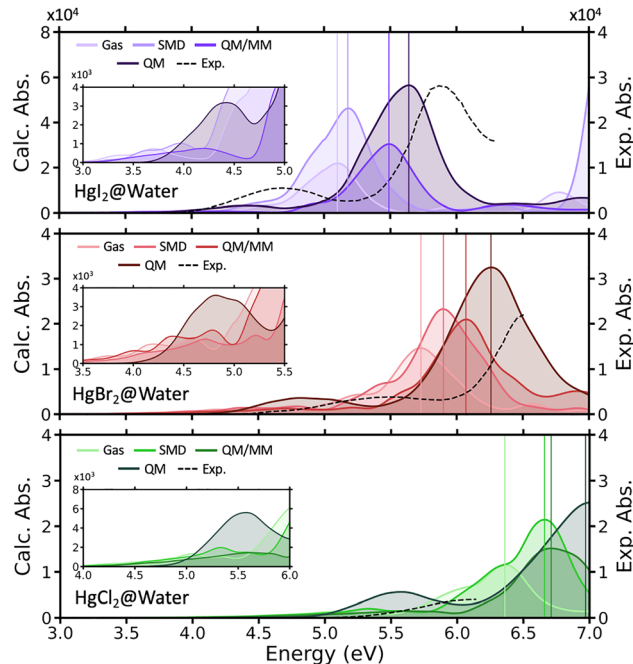


Fig. 4 Calculated absorption spectra of HgI_2 (top), HgBr_2 (middle), and HgCl_2 (bottom) in water, averaged over 300 snapshots taken from AIMD simulations. Spectra were calculated using four approaches to account for solvent effects: (i) gas-phase spectra computed from the same AIMD geometries with the solvent removed (Gas); (ii) spectra obtained using the implicit SMD solvent model (SMD); (iii) spectra calculated using the QM/MM approach, with the solvent described by a force field (QM/MM) and (iv) spectra calculated with the 50 nearest water molecules treated quantum mechanically, combined with the implicit SMD solvent model (QM). The inset shows a magnified view of the first absorption peak of the calculated spectra. For comparison, the experimental absorption spectra measured in water are shown as dotted lines, taken from ref. 67 and 68. Standard deviations of these spectra are shown in Fig. S18, while Fig. S19 displays the calculated gas-phase spectra and their comparison with experiment.

and (iv) full TD-DFT calculations including nearby explicit solvent molecules in the QM region in combination with the SMD model. As illustrated in Fig. 4 and Fig. S12, inclusion of solvent effects *via* the implicit SMD model induces a solvatochromic blue-shift of 0.1–0.4 eV in both major absorption peaks with the increase of absorbance, regardless of the halogen or solvent type. Notably, when nearby solvent molecules were explicitly included in the calculations, the blue shift, which exceeded 0.5 eV, and the increase in absorbance became more pronounced, yielding spectra that more closely matched the experimental measurements. We further performed QM/MM calculations to elucidate the effects of solvent dipole-induced electrostatic interactions and to investigate how the classical treatment of the solvent, relative to a fully QM treatment, influences the absorption spectra of HgX_2 . QM/MM calculations yield an intermediate description between the implicit solvent and fully QM models. In particular, QM/MM significantly improves the predicted peak positions relative to the implicit SMD model, indicating that electrostatic short-range nonbonded interactions are essential for capturing the energetic shifts. It



should be noted, however, that these QM/MM results are obtained from geometries sampled at the fully QM level, and therefore partially inherit solvent-induced polarization and charge-redistribution effects already present in the underlying AIMD trajectories. Nevertheless, the absorption intensities obtained from QM/MM remain systematically lower than those from the full QM treatment, suggesting that solvent–solute CT character and strong electronic coupling, which are not fully captured in the QM/MM framework, play a critical role in determining the spectral intensities. These results demonstrate that while QM/MM provides a substantial improvement over implicit solvent models, an explicit, quantum-mechanical treatment of the local solvent environment is crucial for accurately reproducing both the energetic shifts and intensities observed in the experimental absorption spectra. Still, even with full QM treatment, our calculated spectra show a red shift of 0.2 to 0.5 eV compared to previous theoretical predictions (CASPT2/PCM level of theory) and experimental measurements.^{17,62,63} This systematic deviation likely arises from the molecular structures of HgX₂ extracted from the AIMD simulations, showing slightly elongated Hg–X bonds than previous reports. Therefore, when predicting the absorption spectra of HgX₂, both explicit treatment of the solvent environment and an accurate description of the Hg–X bond length are essential for reliably predicting the peak positions. Achieving a more accurate sampling of equilibrium geometries, whether through properly calibrated force fields, an appropriate multiscale framework, or the incorporation of hybrid functionals, represents an important direction for future work.

To confirm the role of structural sampling on the spectral outcome, we calculated the spectra of HgX₂s using two sets of geometries: one sampled from a Wigner distribution, representing structures around the linear gas-phase geometry, and the other from AIMD snapshots, reflecting geometrical fluctuations in solution (Fig. S13). Regardless of the type of halogen and the type of solvent, absorption spectra computed from structures sampled *via* AIMD snapshots show a significant red-shift of approximately 0.5 eV compared to those obtained from the geometries sampled with Wigner distribution. This highlights the strong influence of solvent-induced structural distortions, such as bond elongation and deviations from linearity, on lowering the electronic excitation energies. Taken together, these results highlight the dual influence of solvation: while the dielectric solvent environment induces a pronounced blue-shift of more than 0.5 eV, the structural distortions caused by explicit solvation counteract this effect by driving the spectrum to lower energies, thereby partially offsetting the blue-shift. This underscores the decisive role of solvation in shaping the excited state energetics and shows that, under realistic conditions such as those encountered in Arctic environments, HgX₂ cannot be meaningfully described as an isolated species. Instead, its photophysics are inherently dictated by solvent complexation and are inseparable from the surrounding medium. Additionally, gas-phase spectra based on AIMD snapshots display pronounced vibronic features, reflecting the broader distribution of molecular geometries sampled in AIMD

compared to those generated by the Wigner distribution. This result indicates that explicit treatment of solvent molecules in the TD-DFT calculations led to suppression of the vibronic features. Notably, when solvent molecules are treated explicitly in the TD-DFT calculations, these vibronic features are largely suppressed, most likely because the manifold of solvent-to-solute CT states with finite oscillator strength introduces substantial spectral broadening that masks the underlying vibronic structure.

Finally, given the strong spin–orbit coupling (SOC), which is a key feature of molecules containing heavy elements, we investigated its influence on the electronic structure and absorption spectra of HgX₂ complexes. Strong SOC can significantly alter the character of excited states by introducing mixing between singlet and triplet states, converting SF triplet states into SO states that exhibit mixed singlet–triplet character with allowed optical transitions. As shown in Fig. S14–S15 and Table S4, HgI₂ exhibits pronounced singlet–triplet mixing. We expect this strong electronic state mixing gives rise to the observed red-shift and enhanced intensity of the first absorption peak. The influence of SOC diminishes as the halogen becomes lighter, and in the case of HgBr₂, the spectra computed with and without SOC are nearly identical. This halogen-dependent trend persists in MeOH, which shows stronger solvent-to-solute CT character than water, suggesting that the dominant factor influencing SOC in the absorption spectra is the type of halogen, rather than the solvent environment. Our results are consistent with the study by Sitkiewicz *et al.*, which reported that mixed-halogen mercury dihalides compounds (HgXY) containing iodine show singlet–triplet mixing and red-shifted behavior due to the large SOC.⁶⁴

In summary, three key factors govern the absorption spectra of HgX₂ in solution: (i) solvation of the HgX₂ molecule in a protic solvent induces a blue-shift; (ii) structural distortions in solution, such as Hg–X bond elongation and deviations from linearity in the X–Hg–X angle, produce a pronounced red-shift, which partially counteracts the blue-shift noted in (i); and (iii) strong SOC produces significant red-shift and intensity enhancement in the absorption spectra of HgI₂, particularly in the first peak, while its effect becomes progressively weaker for lighter halogens.

Solvent-to-solute charge-transfer character of HgX₂

As mentioned in the previous section, we found that solvent nonbonding orbitals can contribute significantly to the electronic absorption spectra of HgX₂. To quantify this effect, we analyzed the excitation character of HgX₂ in solution using 1-TDM analysis, classifying the LE transitions occurring within either the solvent or the solute, and CT transitions between them. Fig. 5 shows the corresponding LE and CT character in each electronic state, together with the calculated absorption spectra of HgI₂ and HgBr₂ in water and MeOH. In all cases, independent of the halogen or solvent, the first absorption band arises mainly from a solute-centered LE transition of (n, σ^*) character within HgX₂, while contributions from solvent-to-solute CT transitions are negligible. On the contrary,



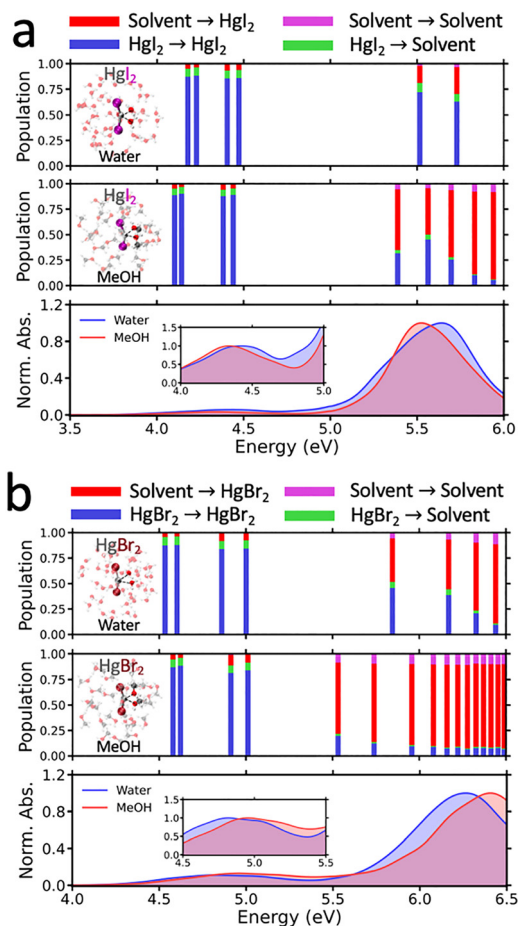


Fig. 5 One-electron transition density matrix (1-TDM) analysis of (a) HgI_2 and (b) HgBr_2 in water and MeOH. The systems were partitioned into two fragments: solute and solvent, and the fractional excitation character between these fragments was quantified. The upper panel (water) and middle panel (MeOH) depict the electronic state energies together with the corresponding excitation character between solute and solvent. The bottom panel shows the calculated absorption spectra in both solvents, where transition energies were averaged over 300 AIMD snapshots. For clarity, in the absorption spectra, an enlarged view of the first peak is provided as an inset. The results of the 1-TDM analysis of HgCl_2 in water are shown in Fig. S20.

in the second absorption peak, strong solute–solvent interactions in solution alter the nature of the transition compared to the gas phase, enhancing the solvent-to-solute CT contribution. Our calculations indicate that the solvent-to-solute CT contribution is stronger for lighter halogens compared to heavier ones, and in MeOH relative to water. We can trace this behavior to the electronic coupling between the $(\sigma, \sigma^*)/\text{XMCT}$ transition of HgX_2 and the (n, σ^*) transition of solvent molecules. We note that bulk MeOH exhibits an (n, σ^*) transition at 6.7 eV (185 nm) which lies closer to the second absorption band of HgI_2 (~ 5.6 eV) and HgBr_2 (~ 6.2 eV) than does water, whose (n, σ^*) transition occurs at 7.4 eV (167 nm). In fact, the second absorption peak of HgBr_2 is blue-shifted by ~ 0.5 eV relative to that of HgI_2 , closely located to the energy region of (n, σ^*) transition of the solvent. Therefore, we conclude that reduced energetic separation between solute and solvent transitions

facilitates stronger electronic coupling, accounting for the enhanced CT character observed in MeOH compared to water, and in Br relative to I. We note that the solvent-to-solute CT trends discussed here are robust with respect to moderate variations in the Hg–X bond length, and are only marginally affected by the slight bond elongation typically introduced by the PBE-based AIMD structures (Fig. S16).

Unlike in the gas phase, where HgX_2 predominantly undergoes direct photodissociation to form neutral HgX^* species, the pronounced CT character in solution, most evident in the second absorption band, suggests that excitation in this region can lead to dissociation into partially or fully reduced species (e.g., $\text{HgX}^{\delta-}$ or HgX^-). The formation of such unstable anionic intermediates could accelerate further photoreduction in solution relative to the gas phase, ultimately promoting the production of $\text{Hg}(0)$, which is abundant in the atmosphere. Also, as mentioned in previous section, compared to Hg atoms in gas-phase HgX_2 , those in solvated HgX_2 show much less positive character due to strong solute–solvent interactions. As a result, significantly enhanced reduction is anticipated under solution than the gas phase.

Overall, our combined AIMD simulations and electronic structure calculations reveal that HgX_2 molecules acquire partial negative charges through interactions with the surrounding solvent molecules. Upon irradiation with sunlight, particularly when the molecule is excited into the second absorption band in the deep-UV region, which exhibits solvent-to-solute CT character, the photoreduction of Hg species can be significantly accelerated. These accumulated partial negative charges in the ground state, along with the enhanced absorption cross-section and the associated solvent-to-solute CT character increase electron density on HgX_2 , thereby facilitating faster photoreduction in aqueous environments compared to the gas phase. The enhanced solvent-to-solute CT character of HgX_2 in polar solvents is expected to promote the formation of HgX^* or direct $\text{Hg}(\text{II}) \rightarrow \text{Hg}(0)$ reduction. By accelerating the initial photochemical step, this effect increases the availability of HgX^* intermediates, whose subsequent photolysis has been shown to extend the effective atmospheric lifetime of mercury.⁶⁴ The excitation-energy-dependent dynamics predicted here suggest that future time-resolved experiments employing different pump energies, selectively addressing distinct absorption bands, could directly probe the solvent-governed photoreduction pathways of HgX_2 in solution.

Conclusions

In this study, we show that Hg–solvent interactions strongly govern the structural and optical properties of HgX_2 in solution. Strong coordination by solvent molecules bends the X–Hg–X angle and drives excess charge localization on HgX_2 . Electronic structure calculations with full quantum mechanical treatment of nearby solvent molecules reveal that the solvent environment reshapes the absorption spectrum through combined electrostatic and geometric effects, and introduces a previously



overlooked solvent-to-solute CT character in the second absorption band. By quantitatively assessing this CT contribution, we show that excitation into these states increases electron density at the Hg center, identifying key factors that promote the accelerated photoreduction of Hg(II) in solution. These results underscore the importance of explicitly accounting for solvation in excited state calculations, a procedure still uncommon due to its high computational cost, yet shown here to be essential for capturing the photophysics of HgX₂ in solution phase. By providing atomistic insight into these processes, our work bridges the molecular-scale description of solvation with the macroscopic photochemical behavior of mercury in aqueous environments. Beyond mercury, these insights can be extended to a wider class of toxic and photoactive systems, underlining how solvent coordination and solvent-to-solute CT can be harnessed both to understand environmental processes and to design functional complex materials with tailored light-driven properties.

Author contributions

Conceptualization: D. I., A. S., H. I.; data curation: D. I., A. S.; formal analysis: D. I., A. S.; funding acquisition: H. I.; investigation: D. I., A. S., H. I.; methodology: D. I., A. S.; software: D. I., A. S.; supervision: H. I.; validation: D. I., A. S.; visualization: D. I.; writing – original draft: D. I., A. S.; writing – review & editing: D. I., A. S., H. I.

Conflicts of interest

The authors declare no conflict of interests.

Data availability

The data supporting this article have been included as part of the supplementary information (SI). Supplementary information: figures and tables for the experimental and theoretical datas. See DOI: <https://doi.org/10.1039/d5cp04729c>.

Acknowledgements

This work was supported by the Institute for Basic Science (IBS-R033). We thank the IBS Research Solution Center (RSC) for supporting computational resources.

Notes and references

- P. A. Ariya, M. Amyot, A. Dastoor, D. Deeds, A. Feinberg, G. Kos, A. Poulain, A. Ryjkov, K. Semeniuk, M. Subir and K. Toyota, *Chem. Rev.*, 2015, **115**, 3760–3802.
- A. Saiz-Lopez, C. A. Cuevas, A. U. Acuña, J. A. Añel, A. S. Mahajan, L. De La Torre, W. Feng, J. Z. Dávalos, D. Roca-Sanjuán, D. E. Kinnison, J. Carmona-García, R. P. Fernandez, Q. Li, J. E. Sonke, A. Feinberg, J. C. G. Martín, J. Villamayor, P. Zhang, Y. Zhang, C. S. Blaszczak-Boxe, O. Travnikov, F. Wang, J. Bieser, J. S. Francisco and J. M. C. Plane, *Sci. Adv.*, 2025, **11**, eads1459.
- A. Dastoor, S. J. Wilson, O. Travnikov, A. Ryjkov, H. Angot, J. H. Christensen, F. Steenhuisen and M. Muntean, *Sci. Total Environ.*, 2022, **839**, 156213.
- N. Pirrone, S. Cinnirella, X. Feng, R. B. Finkelman, H. R. Friedli, J. Leaner, R. Mason, A. B. Mukherjee, G. B. Stracher, D. G. Streets and K. Telmer, *Atmos. Chem. Phys.*, 2010, **10**, 5951–5964.
- I. Cheng, A. Cole, L. Zhang and A. Steffen, *Atmos. Chem. Phys.*, 2025, **25**, 8591–8611.
- R. P. Mason, W. F. Fitzgerald and F. M. M. Morel, *Geochim. Cosmochim. Acta*, 1994, **58**, 3191–3198.
- J. Kuss, N. Wasmund, G. Nausch and M. Labrenz, *Environ. Sci. Technol.*, 2015, **49**, 11449–11457.
- M. E. Goodsite, J. M. C. Plane and H. Skov, *Environ. Sci. Technol.*, 2004, **38**, 1772–1776.
- C. D. Holmes, D. J. Jacob and X. Yang, *Geophys. Res. Lett.*, 2006, **33**, 2006GL027176.
- L. Wang, J. Yan, A. Saiz-Lopez, B. Jiang, F. Yue, X. Yu and Z. Xie, *Sci. Total Environ.*, 2022, **834**, 155030.
- R. P. Fernandez, A. Carmona-Balea, C. A. Cuevas, J. A. Barrera, D. E. Kinnison, J. Lamarque, C. Blaszczak-Boxe, K. Kim, W. Choi, T. Hay, A. Blechschmidt, A. Schönhardt, J. P. Burrows and A. Saiz-Lopez, *J. Adv. Model. Earth Syst.*, 2019, **11**, 2259–2289.
- J. C. Gómez Martín, A. Saiz-Lopez, C. A. Cuevas, A. R. Baker and R. P. Fernández, *J. Geophys. Res. Atmos.*, 2022, **127**, e2021JD036081.
- A. Saiz-Lopez, R. P. Fernandez, C. Ordóñez, D. E. Kinnison, J. C. Gómez Martín, J.-F. Lamarque and S. Tilmes, *Atmos. Chem. Phys.*, 2014, **14**, 13119–13143.
- S. L. Bager, L. Zamok, S. P. A. Sauer and M. S. Johnson, *J. Phys. Chem. A*, 2026, **130**, 1162–1174.
- M. Costa, *Sci. Total Environ.*, 2000, **261**, 125–135.
- A. Saiz-Lopez, A. U. Acuña, A. S. Mahajan, J. Z. Dávalos, W. Feng, D. Roca-Sanjuán, J. Carmona-García, C. A. Cuevas, D. E. Kinnison, J. C. Gómez Martín, J. S. Francisco and J. M. C. Plane, *Geophys. Res. Lett.*, 2022, **49**, e2022GL097953.
- J. Carmona-García, A. Saiz-Lopez, A. S. Mahajan, F. Wang, A. Borrego-Sánchez, A. U. Acuña, C. A. Cuevas, J. Z. Dávalos, A. Feinberg, A. Spolaor, M. F. Ruiz-López, J. S. Francisco and D. Roca-Sanjuán, *Proc. Natl. Acad. Sci. U. S. A.*, 2025, **122**, e2422885122.
- H. Hofmann and S. R. Leone, *J. Chem. Phys.*, 1978, **69**, 3819–3825.
- M. Lim, M. F. Wolford, P. Hamm and R. M. Hochstrasser, *Chem. Phys. Lett.*, 1998, **290**, 355–362.
- N. Pugliano, A. Z. Szarka, S. Gnanakaran, M. Triechel and R. M. Hochstrasser, *J. Chem. Phys.*, 1995, **103**, 6498–6511.
- N. Pugliano, D. K. Palit, A. Z. Szarka and R. M. Hochstrasser, *J. Chem. Phys.*, 1993, **99**, 7273–7276.
- J. H. Lee, T. K. Kim, J. Kim, Q. Kong, M. Cammarata, M. Lorenc, M. Wulff and H. Ihee, *J. Am. Chem. Soc.*, 2008, **130**, 5834–5835.



- 23 J. G. Kim, T. W. Kim, J. Kim and H. Ihee, *Acc. Chem. Res.*, 2015, **48**, 2200–2208.
- 24 E. H. Choi, Y. Lee, J. Heo and H. Ihee, *Chem. Sci.*, 2022, **13**, 8457–8490.
- 25 V. Markmann, J. Pan, B. L. Hansen, M. L. Haubro, A. Nimmrich, P. Lenzen, M. Levantino, T. Katayama, S. Adachi, S. Gorski-Bilke, F. Temps, A. O. Dohn, K. B. Møller, M. M. Nielsen and K. Haldrup, *Chem. Sci.*, 2024, **15**, 11391–11401.
- 26 K. H. Kim, J. H. Lee, J. Kim, S. Nozawa, T. Sato, A. Tomita, K. Ichiyanagi, H. Ki, J. Kim, S. Adachi and H. Ihee, *Phys. Rev. Lett.*, 2013, **110**, 165505.
- 27 Q. Kong, J. H. Lee, A. Plech, M. Wulff, H. Ihee and M. H. J. Koch, *Angew. Chem., Int. Ed.*, 2008, **47**, 5550–5553.
- 28 Y. Lee, K. Y. Oang, D. Kim and H. Ihee, *Struct. Dyn.*, 2024, **11**, 031301.
- 29 T. K. Kim, M. Lorenc, J. H. Lee, M. Lo Russo, J. Kim, M. Cammarata, Q. Kong, S. Noel, A. Plech, M. Wulff and H. Ihee, *Proc. Natl. Acad. Sci. U. S. A.*, 2006, **103**, 9410–9415.
- 30 S. Jun, J. H. Lee, J. Kim, J. Kim, K. H. Kim, Q. Kong, T. K. Kim, M. Lo Russo, M. Wulff and H. Ihee, *Phys. Chem. Chem. Phys.*, 2010, **12**, 11536.
- 31 D. Leshchev, D. Khakhulin, G. Newby, H. Ki, H. Ihee and M. Wulff, *J. Chem. Phys.*, 2019, **151**, 054310.
- 32 L. Martínez, R. Andrade, E. G. Birgin and J. M. Martínez, *J. Comput. Chem.*, 2009, **30**, 2157–2164.
- 33 S. Nosé, *J. Chem. Phys.*, 1984, **81**, 511–519.
- 34 W. G. Hoover, *Phys. Rev. A: At., Mol., Opt. Phys.*, 1985, **31**, 1695–1697.
- 35 S. Grimme, J. Antony, S. Ehrlich and H. Krieg, *J. Chem. Phys.*, 2010, **132**, 154104.
- 36 J. P. Perdew, K. Burke and M. Ernzerhof, *Phys. Rev. Lett.*, 1996, **77**, 3865–3868.
- 37 J. VandeVondele and J. Hutter, *J. Chem. Phys.*, 2007, **127**, 114105.
- 38 T. D. Kühne, M. Iannuzzi, M. Del Ben, V. V. Rybkin, P. Seewald, F. Stein, T. Laino, R. Z. Khaliullin, O. Schütt, F. Schiffmann, D. Golze, J. Wilhelm, S. Chulkov, M. H. Bani-Hashemian, V. Weber, U. Borštnik, M. TAILLEFUMIER, A. S. Jakobovits, A. Lazzaro, H. Pabst, T. Müller, R. Schade, M. Guidon, S. Andermatt, N. Holmberg, G. K. Schenter, A. Hehn, A. Bussy, F. Belleflamme, G. Tabacchi, A. Glöß, M. Lass, I. Bethune, C. J. Mundy, C. Plessl, M. Watkins, J. VandeVondele, M. Krack and J. Hutter, *J. Chem. Phys.*, 2020, **152**, 194103.
- 39 P.-O. Widmark, P.-Å. Malmqvist and B. O. Roos, *Theor. Chim. Acta*, 1990, **77**, 291–306.
- 40 N. Forsberg and P.-Å. Malmqvist, *Chem. Phys. Lett.*, 1997, **274**, 196–204.
- 41 B. A. Heß, C. M. Marian, U. Wahlgren and O. Gropen, *Chem. Phys. Lett.*, 1996, **251**, 365–371.
- 42 M. Reiher, *Theor. Chem. Acc.*, 2006, **116**, 241–252.
- 43 F. Aquilante, R. Lindh and T. Bondo Pedersen, *J. Chem. Phys.*, 2007, **127**, 114107.
- 44 G. Li Manni, I. Fdez. Galván, A. Alavi, F. Aleotti, F. Aquilante, J. Autschbach, D. Avagliano, A. Baiardi, J. J. Bao, S. Battaglia, L. Birnoschi, A. Blanco-González, S. I. Bokarev, R. Broer, R. Cacciari, P. B. Calio, R. K. Carlson, R. Carvalho Couto, L. Cerdán, L. F. Chibotaru, N. F. Chilton, J. R. Church, I. Conti, S. Coriani, J. Cuéllar-Zuquin, R. E. Daoud, N. Dattani, P. Decleva, C. De Graaf, M. G. Delcey, L. De Vico, W. Dobrautz, S. S. Dong, R. Feng, N. Ferré, M. Filatov(Gulak), L. Gagliardi, M. Garavelli, L. González, Y. Guan, M. Guo, M. R. Hennefarth, M. R. Hermes, C. E. Hoyer, M. Huix-Rotllant, V. K. Jaiswal, A. Kaiser, D. S. Kaliakin, M. Khamesian, D. S. King, V. Kochetov, M. Krośnicki, A. A. Kumaar, E. D. Larsson, S. Lehtola, M.-B. Lepetit, H. Lischka, P. López Ríos, M. Lundberg, D. Ma, S. Mai, P. Marquetand, I. C. D. Merritt, F. Montorsi, M. Mörchen, A. Nenov, V. H. A. Nguyen, Y. Nishimoto, M. S. Oakley, M. Olivucci, M. Oppel, D. Padula, R. Pandharkar, Q. M. Phung, F. Plasser, G. Raggi, E. Rebolini, M. Reiher, I. Rivalta, D. Roca-Sanjuán, T. Romig, A. A. Safari, A. Sánchez-Mansilla, A. M. Sand, I. Schapiro, T. R. Scott, J. Segarra-Martí, F. Segatta, D.-C. Sergentu, P. Sharma, R. Shepard, Y. Shu, J. K. Staab, T. P. Straatsma, L. K. Sørensen, B. N. C. Tenorio, D. G. Truhlar, L. Ungur, M. Vacher, V. Veryazov, T. A. Voß, O. Weser, D. Wu, X. Yang, D. Yarkony, C. Zhou, J. P. Zobel and R. Lindh, *J. Chem. Theory Comput.*, 2023, **19**, 6933–6991.
- 45 T. Yanai, D. P. Tew and N. C. Handy, *Chem. Phys. Lett.*, 2004, **393**, 51–57.
- 46 D. Peng and M. Reiher, *J. Chem. Phys.*, 2012, **136**, 244108.
- 47 A. V. Marenich, C. J. Cramer and D. G. Truhlar, *J. Phys. Chem. B*, 2009, **113**, 6378–6396.
- 48 R. Crespo-Otero and M. Barbatti, *Theor. Chem. Acc.*, 2012, **131**, 1237.
- 49 F. Neese, *Wiley Interdiscip. Rev.: Comput. Mol. Sci.*, 2012, **2**, 73–78.
- 50 F. Plasser, *J. Chem. Phys.*, 2020, **152**, 084108.
- 51 B. C. Shepler, A. D. Wright, N. B. Balabanov and K. A. Peterson, *J. Phys. Chem. A*, 2007, **111**, 11342–11349.
- 52 I. Persson, *Pure Appl. Chem.*, 1986, **58**, 1153–1161.
- 53 M. Hargittai, *Chem. Rev.*, 2000, **100**, 2233–2302.
- 54 M. Busato, G. Fazio, F. Tavani, S. Pollastri and P. D'Angelo, *Phys. Chem. Chem. Phys.*, 2022, **24**, 18094–18102.
- 55 J. Hernández-Cobos, A. Ramírez-Solís, L. Maron and I. Ortega-Blake, *J. Chem. Phys.*, 2012, **136**, 014502.
- 56 L. Castro, A. Dommergue, A. Renard, C. Ferrari, A. Ramirez-Solis and L. Maron, *Phys. Chem. Chem. Phys.*, 2011, **13**, 16772.
- 57 I. Persson, M. Sandström and P. L. Goggin, *Inorg. Chim. Acta*, 1987, **129**, 183–197.
- 58 M. Sandström and S. Ahrlund, *Acta Chem. Scand.*, 1978, **32**, 607–625.
- 59 I. Persson, *Polyhedron*, 2018, **139**, 222–228.
- 60 D. N. Waters and Z. Kantarci, *J. Raman Spectrosc.*, 1977, **6**, 251–256.
- 61 I. Persson, M. Sandström, P. L. Goggin and A. Mosset, *J. Chem. Soc., Dalton Trans.*, 1985, **0**, 1597–1604.
- 62 T. R. Griffiths and R. A. Anderson, *J. Chem. Soc., Faraday Trans. 2*, 1979, **75**, 957.



- 63 T. R. Griffiths and R. A. Anderson, *Inorg. Chem.*, 1979, **18**, 2506–2511.
- 64 A. Saiz-Lopez, A. U. Acuña, T. Trabelsi, J. Carmona-García, J. Z. Dávalos, D. Rivero, C. A. Cuevas, D. E. Kinnison, S. P. Sitkiewicz, D. Roca-Sanjuán and J. S. Francisco, *J. Am. Chem. Soc.*, 2019, **141**, 8698–8702.
- 65 S. P. Sitkiewicz, D. Rivero, J. M. Oliva-Enrich, A. Saiz-Lopez and D. Roca-Sanjuán, *Phys. Chem. Chem. Phys.*, 2019, **21**, 455–467.
- 66 J. Maya, *J. Chem. Phys.*, 1977, **67**, 4976–4980.
- 67 T. R. Griffiths and R. A. Anderson, *J. Chem. Soc., Faraday Trans.*, 1990, **86**, 1425–1435.
- 68 V. I. Belevantsev, V. I. Malkova, L. V. Gushchina and A. A. Obolenskii, *Russ. J. Coord. Chem.*, 2004, **30**, 465–472.
- 69 R. Z. Deyanov, K. P. Petrov, V. V. Ugarov, B. M. Shchedrin and N. G. Rambidi, *J. Struct. Chem.*, 1986, **26**, 698–703.
- 70 R. Åkesson, I. Persson, M. Sandström and U. Wahlgren, *Inorg. Chem.*, 1994, **33**, 3715–3723.

